INTERNATIONAL JOURNAL OF
NUMERICAL ANALYSIS AND MODELING
Volume 9, Number 3, Pages 479–504

© 2012 Institute for Scientific
Computing and Information

A MULTIRESOLUTION METHOD FOR THE SIMULATION OF SEDIMENTATION IN INCLINED CHANNELS

RAIMUND BÜRGER, RICARDO RUIZ-BAIER, KAI SCHNEIDER, AND HÉCTOR TORRES

Abstract. An adaptive multiresolution scheme is proposed for the numerical solution of a spatially two-dimensional model of sedimentation of suspensions of small solid particles dispersed in a viscous fluid. This model consists in a version of the Stokes equations for incompressible fluid flow coupled with a hyperbolic conservation law for the local solids concentration. We study the process in an inclined, rectangular closed vessel, a configuration that gives rise a well-known increase of settling rates (compared with a vertical vessel) known as the "Boycott effect". Sharp fronts and discontinuities in the concentration field are typical features of sedimentation phenomena. This solution behavior calls for locally refined meshes to concentrate computational effort on zones of strong variation. The spatial discretization presented herein is naturally based on a finite volume (FV) formulation for the Stokes problem including a pressure stabilization technique, while a Godunov-type scheme endowed with a fully adaptive multiresolution (MR) technique is applied to capture the evolution of the concentration field, which in addition induces an important speed-up of CPU time and savings in memory requirements. Numerical simulations illustrate that the proposed scheme is robust and allows for substantial reductions in computational effort while the computations remain accurate and stable.

Key words. Two-dimensional sedimentation, transport-flow coupling, Boycott effect, space adaptivity, multiresolution analysis, finite volume approximation

1. Introduction

1.1. Scope. Sedimentation is a widely employed method for the solid-liquid separation of suspensions in mineral processing, chemical engineering, wastewater treatment, the pulp-and-paper industries, and other applications. Finely divided particles are allowed to settle under the effect of gravity to produce the desired separation of the suspension into a clear supernatant liquid and a consolidated sediment. A widely accepted spatially one-dimensional sedimentation model [35] gives rise to one scalar, nonlinear hyperbolic conservation law for the solids concentration as a function of depth and time. This paper deals with an extension of this model to two space dimensions, which entails the necessity to solve additional equations (here, a variant of the Stokes system) for the flow field of the mixture. (In one space dimension, this flow field is determined by boundary conditions, and vanishes for batch settling in a closed column.) In particular, we study numerically the sedimentation of particles in a rectangular channel that is inclined to enhance the process of settling [2, 55]. The enhancement of settling rates was first reported by Boycott [8], and this phenomenon is usually referred to as "Boycott effect".

We assume that the particles are of spherical shape, equal size and density and do not aggregate, and that sedimentation starts from uniformly distributed particles in an incompressible Newtonian fluid, which is initially at rest. The equations are expressed in terms of the divergence-free volume average velocity of the mixture, which gives rise to a version of the Stokes system. The final system of two-dimensional, time-dependent governing equations consists in one scalar hyperbolic conservation law for the solids concentration, coupled with the Stokes equations for

---

Received by the editors February 19, 2011 and, in revised form, May 1, 2011.
2000 *Mathematics Subject Classification.* 65M08, 65M50, 76D99.

the volume average velocity of the mixture and pressure. The governing equations are a special, reduced case of a model that could also be based on the Navier-Stokes instead of the Stokes equations, and include additional degenerating nonlinear diffusive terms modeling sediment compressibility, an effect which is not considered herein. (For details on the model formulation and the underlying assumptions we refer to [4, 17, 39].) On the other hand, the simple rectangular geometry of the model greatly facilitates the implementation of the numerical method; since the model is well studied we may assess whether numerical results are correct.

It is the purpose of this paper to provide a useful technique to obtain accurate numerical solutions of the coupled system by an adaptive multiresolution (MR) approach. In such a method, a coarse mesh is adapted (by local refinement) during the computational procedure only in regions of steep variation of the flow or concentration quantities. In particular, we focus on the variation of the volume fraction (or concentration) field. In contrast to the original work by Harten [32], and following [21], a *fully* adaptive approach will be applied here, in which the space-adaptive scheme acts on the image of the compressing operator, and not on the finest grid. Mesh refinement is realized through the division of mesh elements into smaller ones (sons) by dividing the corresponding edges and inserting new nodes at their midpoints. The original parent control volumes and parent edges are deactivated and the computational algorithm uses only the (non-divided) active elements. Since our MR method is defined on the basis of a FV scheme, it is locally conservative by construction. This property is highly desirable for the simulation of the studied phenomenon. Another advantage of FV schemes in comparison with other discretization approaches, is that the unknowns are approximated by piecewise constant functions. Numerical examples illustrate the performance of the method.

1.2. Related work. Introductions to the modeling of sedimentation processes that lead to the present model (or variants of it) can be found in [13, 17, 18, 23, 60, 61]. The Boycott effect is exploited in numerous devices that are employed in industry to accelerate the sedimentation of solid particles from solid-liquid suspension, mainly because the production rate of clarified fluid is in general, higher than that of fluid obtained from vertically oriented vessels. This phenomenon has attracted considerable interest and was studied experimentally [44, 45, 47, 54, 58, 63], theoretically [7, 34, 56, 57] and computationally [36, 37]. (These lists of references are far from being complete). The first attempt to explain this effect theoretically and to quantify the increase in settling rate (i.e., the rate of production of clear liquid from an initially homogeneous suspension) was advanced by Ponder [48] and Nakamura and Kuroda [42] ("PNK theory"). Their simple kinematic theory is based on the increase of horizontal settling area due to the inclination of the channel (compared with a vertical orientation). It has long been known that PNK theory produces an acceptable approximation only under idealizing assumptions, and mostly over-predicts the increase in settling rate [30]. For detailed state-of-the-art explanations and rigorous analyses we refer to [1, 33, 61]. As is pointed out in [61], the main breakthrough in understanding the Boycott effect was the resolution of the thin pure fluid layer streaming beneath the downward-facing inclined wall. It is this fluid layer which is eventually responsible for the increase of settling rates. There are numerous applications of this effect for solid-liquid separation and classification in mineral processing [24, 28, 29, 31], wastewater treatment, volcanology [6], petroleum industry [38, 39], analytical chemistry, and other areas.

Concerning relevant numerical techniques, we mention that Wan et al. [62] proposed an hybrid finite element/FV method for simulating two immiscible flows.

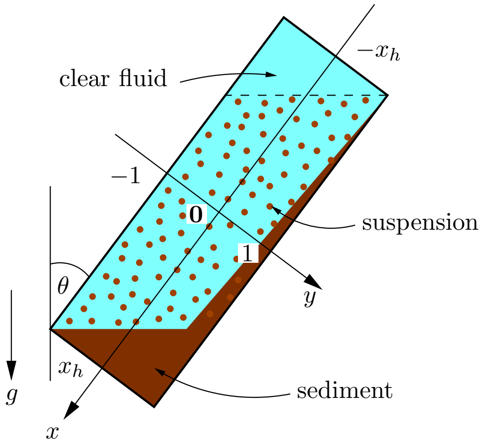

FIGURE 1. Sketch of the settling of a suspension in an inclined vessel at some time $t > 0$.

A similar problem is numerically solved using upwind schemes in [36]. Some industrial applications are presented in [38], where simplified models are used. In [20], the authors model the solid stress of the particulate phase using granular flow theory, and present some numerical evidence. Doroodchi et al. [24] performed several numerical tests using inclined vessels, and moreover they provide some comparisons with experimental data. Nigam [43] proposed a numerical method to accurately capture the mixture-pure fluid interface dynamics present in the Boycott effect. In the past 15 years, several MR methods have been proposed for the numerical study of one-dimensional conservation laws and degenerate parabolic equations [12, 15, 21, 22, 32, 41, 59]. As for MR methods for multidimensional flow problems, since the work of Bihari and Harten [5], the related contributions include [3, 14, 19, 27, 40, 52, 53].

1.3. Outline of the paper. The remainder of the paper is organized as follows. Section 2 contains the main aspects of modeling and the mathematical formulation. In Section 3 we describe the Godunov scheme to approximate the governing equation of the concentration field. Next, Section 4 presents the MR analysis applied to the FV method described in Section 3. In Section 5 we outline a FV method with a pressure stabilization technique for solving the variable-density Stokes problem. A discussion on the coupling strategies and a description of overall algorithms are provided in Section 6, and some numerical examples illustrating the efficiency of our proposed method, the effect of choosing a parameter in the pressure stabilization technique, and the effect of varying the angle of inclination θ, are included in Section 7. We end with some conclusions and a brief discussion on further developments in Section 8.

2. Model of sedimentation

The process of settling of particles in an inclined vessel (or channel) is illustrated in Figure 1, where three regions are clearly defined: the ones occupied by clear fluid, suspension, and sediment, respectively. Here θ represents the angle of inclination of the channel with respect to the vertical direction of gravity. We assume that the sedimentation starts from an initially homogeneous, monodisperse suspension. In terms of non-dimensional components, the conservation law governing the evolution of the concentration field on $\Omega := [-x_h, x_h] \times [-1, 1]$ is given by

$$\frac{\partial \phi}{\partial t} + \nabla \cdot \big(\phi \mathbf{v} + f(\phi)\mathbf{k}\big) = 0, \quad \mathbf{x} := (x, y) \in \Omega, \quad t \in (0, T], \tag{2.1}$$

where t is time, $\mathbf{v}$ is the volume-average velocity of the mixture, ϕ is the local solids volume fraction (with $0 \leq \phi \leq 1$), the vector $\mathbf{k} = (\cos\theta, \sin\theta)^{\mathrm{T}}$ is aligned with the gravity force, and $f(\phi)$ is given by $f(\phi) = \phi V(\phi)$, where $V(\phi)$ is the so-called hindered settling factor (see e.g. [23]). A common choice is the Richardson and Zaki [50] expression $V(\phi) = (1-\phi)^{n_{\mathrm{RZ}}}$ with an exponent $n_{\mathrm{RZ}} \geq 1$.

Equation (2.1) is coupled with the following version of the Stokes system for the velocity $\mathbf{v}$ and the pressure p (for more details see [39]):

$$-\nabla \cdot \big(\mu(\phi)\nabla \mathbf{v}\big) + \lambda \nabla p = \mathbf{f}, \quad \nabla \cdot \mathbf{v} = 0 \quad \text{on } \Omega. \tag{2.2}$$

The concentration-dependent suspension viscosity $\mu(\phi)$ is assumed to be given by the generalized Roscoe-Brinkman law [10, 46, 51] $\mu(\phi) = (1-\phi)^{-\beta}$, $\beta \geq 1$. This relation describes an increase of viscosity of the mixture corresponding to the deposited sediment. The forcing term $\mathbf{f}$ captures local density variations of the suspension, which essentially drive the motion of the mixture. This term is herein given by

$$\mathbf{f} = -\lambda B \phi \mathbf{k} = -\lambda B \phi (\cos\theta, \sin\theta)^{\mathrm{T}},$$

where λ and B are model parameters.

2.1. Boundary and initial conditions.

The Stokes problem (2.2) is complemented with no-slip conditions on the entire boundary,

$$\mathbf{v} = 0 \quad \text{on } \partial\Omega, \tag{2.3}$$

whereas for (2.1) we assume zero-flux conditions on the boundary, or alternatively, the following Dirichlet data:

$$\phi = \begin{cases} 0 & \text{for } x = -x_h \text{ and } y = -1, \\ 1 & \text{for } x = x_h \text{ and } y = 1. \end{cases}$$

The concentration field is assumed to be initially piecewise constant in the whole inclined channel, and to obtain initial velocities and pressures we solve the Stokes system (2.2), (2.3) with the initial concentration as input data.

2.2. Preliminaries and the pressure stabilization for the Stokes system.

We propose to apply a pressure-stabilization-like method (see e.g. [9]), in which a term $\eta^2 \Delta p$ with a regularization parameter $\eta > 0$ is included into the equation of continuity. To this end, let us assume that $\mu(\phi) \in (0, +\infty)$ and $\mathbf{f} \in L^2(\Omega)^2$, and consider the following perturbation of the original Stokes system (2.2), (2.3) for $\mathbf{v} = \mathbf{v}^\eta$ and $p = p^\eta$:

$$\begin{aligned} -\nabla \cdot \big(\mu(\phi)\nabla \mathbf{v}^\eta\big) + \lambda \nabla p^\eta &= \mathbf{f} \quad \text{in} \quad \Omega \subset \mathbb{R}^2, \\ \nabla \cdot \mathbf{v}^\eta &= \eta^2 \Delta p^\eta \quad \text{in} \quad \Omega \subset \mathbb{R}^2, \\ \mathbf{v}^\eta &= 0 \quad \text{on} \quad \partial\Omega. \end{aligned} \tag{2.4}$$

Then, roughly speaking, for bounded values of the perturbed pressure p^η, the divergence of $\mathbf{v}^\eta$ is close to zero (it tends to zero as $\eta \to 0$).

We now give a precise definition of a weak solution to (2.2), (2.3).

Definition 2.1. *Let* $E(\Omega) := \{\mathbf{v} \in H_0^1(\Omega)^2 \mid \operatorname{div} \mathbf{v} = 0\}$*. Then* $(\mathbf{v}, p)$ *is called a* weak solution *of (2.2), (2.3) if* $\mathbf{v} \in E(\Omega)$*,* $p \in L^2(\Omega)$ *with* $\int_\Omega p(\mathbf{x})\,\mathrm{d}\mathbf{x} = 0$*, and*

$$\int_\Omega \mu(\phi)\nabla\mathbf{v} : \nabla\mathbf{u}\,\mathrm{d}\mathbf{x} - \lambda \int_\Omega p(\mathbf{x}) \operatorname{div}\mathbf{u}(\mathbf{x})\,\mathrm{d}\mathbf{x} = \int_\Omega \mathbf{f}(\mathbf{x}) \cdot \mathbf{u}(\mathbf{x})\,\mathrm{d}\mathbf{x} \quad \forall \mathbf{u} \in H_0^1(\Omega)^2,$$

where, as usual, $\nabla\mathbf{v} : \nabla\mathbf{u} = \nabla v^1 \cdot \nabla u^1 + \nabla v^2 \cdot \nabla u^2$*.*

3. Discretization of the concentration equation

To compute an approximate solution of the hyperbolic equation, let us define a mesh, denoted by $\mathcal{T}$, on the rectangular spatial domain Ω consisting of $N_x \cdot N_y$ control volumes Ω_{ij} that satisfy the assumptions stated in the following definition.

Definition 3.1. *(Admissible mesh) An admissible mesh of* Ω*, denoted by* $\mathcal{T}$*, is given by a family* $(\Omega_{ij})_{i=0,\dots,N_x-1;j=0,\dots,N_y-1}$*,* $N_x, N_y \in \mathbb{N}$*, such that*

$$\Omega_{ij} := [x_{i-1/2}, x_{i+1/2}] \times [y_{j-1/2}, y_{j+1/2}],$$

where

$$x_{-1/2} = -x_h < x_0 < x_{1/2} < x_1 < \dots < x_{N_x-1} < x_{N_x-1/2} = x_h,$$
$$y_{-1/2} = -1 < y_0 < y_{1/2} < y_1 < \dots < y_{N_y-1} < y_{N_y-1/2} = 1.$$

For each cell the width in the x*- and* y*- direction is* $\Delta x = 2x_h/N_x$ *and* $\Delta y = 2/N_y$*, respectively.*

The numerical method used for solving (2.1) is based on a classical FV formulation. Let $\mathcal{T}$ be an admissible mesh on Ω (cf. Definition 3.1). We denote by $\phi_{ij}(t)$ the cell average of ϕ on Ω_{ij} at time t, i.e.,

$$\phi_{ij}(t) = \frac{1}{|\Omega_{ij}|} \int_{\Omega_{ij}} \phi(\mathbf{x}, t)\,\mathrm{d}\mathbf{x}, \quad \text{where} \quad |\Omega_{ij}| = \int_{\Omega_{ij}} \mathrm{d}\mathbf{x} = \Delta x \Delta y.$$

We denote by ϕ_{ij}^n the approximate value of $\phi_{ij}(t_n)$, where $t_n = n\Delta t$. By F^1 and F^2 we denote the x- and y-component, respectively, of the flux vector $\mathbf{F}(\phi) = \phi\mathbf{v} + f(\phi)\mathbf{k}$ for a given velocity $\mathbf{v}$, that is,

$$F^1 = \phi v^1 + \phi(1-\phi)^{n_{\mathrm{RZ}}} \cos\theta, \quad F^2 = \phi v^2 + \phi(1-\phi)^{n_{\mathrm{RZ}}} \sin\theta,$$

and let us recall the following definition for the Godunov numerical fluxes:

$$F^1_{i+1/2,j} := \begin{cases} \displaystyle\min_{\phi_{ij}^n \le \phi \le \phi_{i+1,j}^n} F^1(\phi) & \text{if } \phi_{ij}^n \le \phi_{i+1,j}^n, \\ \displaystyle\max_{\phi_{ij}^n \ge \phi \ge \phi_{i+1,j}^n} F^1(\phi) & \text{if } \phi_{ij}^n > \phi_{i+1,j}^n, \end{cases}$$

$$F^2_{i,j+1/2} := \begin{cases} \displaystyle\min_{\phi_{ij}^{n+1/2} \le \phi \le \phi_{i,j+1}^{n+1/2}} F^2(\phi) & \text{if } \phi_{ij}^{n+1/2} \le \phi_{i,j+1}^{n+1/2}, \\ \displaystyle\max_{\phi_{ij}^{n+1/2} \ge \phi \ge \phi_{i,j+1}^{n+1/2}} F^2(\phi) & \text{if } \phi_{ij}^{n+1/2} > \phi_{i,j+1}^{n+1/2}. \end{cases}$$

The numerical scheme to solve (2.1) is a standard conservative Godunov scheme, which is applied here in a direction-wise operator splitting fashion. This scheme can be written as

$$\phi_{ij}^{n+1/2} = \phi_{ij}^n - \frac{\Delta t}{\Delta x}\bigl(F^1_{i+1/2,j} - F^1_{i-1/2,j}\bigr), \tag{3.1}$$

$$\phi_{ij}^{n+1} = \phi_{ij}^{n+1/2} - \frac{\Delta t}{\Delta y}\bigl(F^2_{i,j+1/2} - F^2_{i,j-1/2}\bigr). \tag{3.2}$$

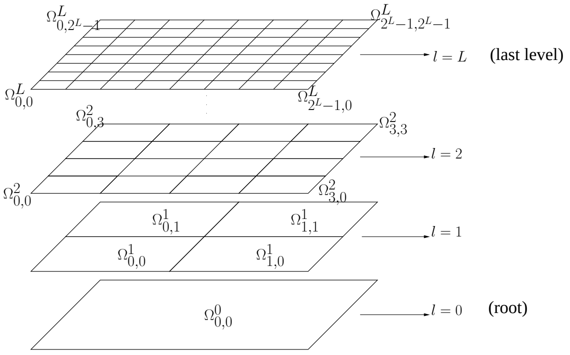

FIGURE 2. Sketch of a family of nested dyadic grids.

To ensure stability we must guarantee that the following CFL condition is satisfied:

$$\max\{|u^1_{\max}|, |u^2_{\max}|\}\Delta t < \frac{1}{2}\min\{\Delta x, \Delta y\}, \tag{3.3}$$

where in each time step, we define

$$u^k_{\max} = \max\left\{ \left| \frac{\mathrm{d}F^k}{\mathrm{d}\phi}(\phi^n_{ij}) \right| \,\middle|\, 0 \le i \le N_x - 1,\ 0 \le j \le N_y - 1 \right\}, \quad k = 1, 2.$$

Since velocity is variable, the first term on the left-hand side should be calculated each time. The time step Δt is chosen adaptively so that the CFL condition (3.3) holds, in particular we consider

$$\Delta t = \frac{\Delta y}{2(\lfloor u_{\max} \rfloor + 1)}, \quad \text{where } u_{\max} = \max\{|u^1_{\max}|, |u^2_{\max}|\}.$$

4. Adaptive multiresolution scheme

The concept of multiresolution (MR) for cell averages is naturally fitted for finite volume (FV) schemes [5, 32, 40]. The rough idea behind this procedure is that we represent a data set given on a fine grid as values on a much coarser grid plus a series of differences at different levels of nested dyadic grids (see Figure 2). These differences are small in regions where the solution is smooth and contain information on the local regularity of the solution. Therefore, by means of a thresholding operation, data compression is achieved [5, 15].

4.1. Data structure.

Definition 4.1 (Nested two-dimensional dyadic grids)**.** *We define a sequence* $\mathcal{T}^l$, $0 \le l \le L$, *of nested, dyadically coarsened grids in the following recursive manner. We define* $\mathcal{T}^l := (\Omega^l_{ij})_{i,j=0,\dots,2^l-1}$, $0 \le l \le L$. *The finite volume* Ω^l_{ij} *has the four sons (see Figure 2)* $\Omega^{l+1}_{2i,2j}$, $\Omega^{l+1}_{2i+1,2j}$, $\Omega^{l+1}_{2i,2j+1}$ *and* $\Omega^{l+1}_{2i+1,2j+1}$. *Each mesh* $\mathcal{T}^l$ *is a mesh in the sense of Definition 3.1 with* $N_x \cdot N_y$ *elements, where* $N_x = N_y = 2^l$. *Moreover,* $\mathcal{T}^0 = \Omega^0_{0,0}$ *is the root and* $\mathcal{T}^L$ *is the finest mesh.*

Another key element of MR devices is a suitable framework for the storage of the solution. In our case, we use a two-dimensional graded tree, or quad-tree (see e.g. [14, 21, 52]). As usual in the mentioned context, the *root* is the basis of the tree; and a *node* is an element of the tree, which represents a control volume on a local mesh. A *parent node* has 4 sons, and the sons of the same parent are called *brothers.* A given node has s' nearest neighbors in each direction, called the nearest

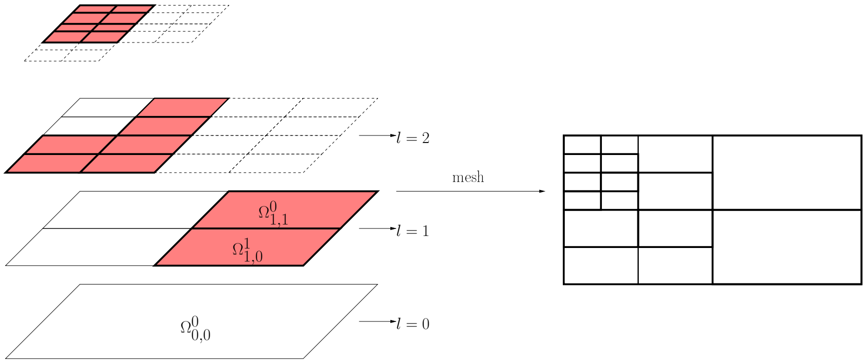

FIGURE 3. Sketch of a graded tree structure in 2D.

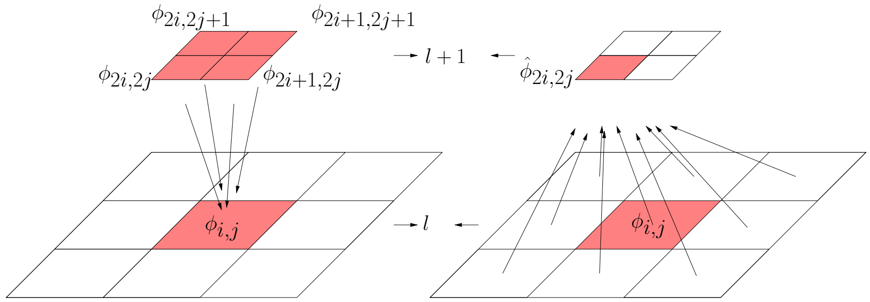

FIGURE 4. Sketch of the action of the projection operator (left) and prediction operator (right) for navigating through the graded tree.

cousins; and for a given child node, the nearest cousins of the parent node are called the nearest *uncles*. A node is called a *leaf* when it has no children, and a node has always s' (in our case $s' = 1$) nearest uncles in each direction, diagonal included (see Figure 3).

4.2. Transfer operators and multiresolution transform. We denote by Λ the index set of the existing nodes, by $\mathcal{L}(\Lambda)$ the restriction of Λ to the leaves, and by Λ_l the restriction of Λ to a level l, $0 \leq l < L$. The navigation through the different levels of the tree is done by two operators. First, to estimate the cell average at a level l from those of the next finer level $l+1$, we use the *projection operator* $\mathrm{P}_{l+1\to l} : \phi^{l+1} \to \phi^{l}$, which is defined by

$$\phi^l_{ij} = \big(P_{l+1\to l}(\phi^{l+1})\big)_{ij} := \frac{1}{4}\left(\phi^{l+1}_{2i,2j} + \phi^{l+1}_{2i+1,2j} + \phi^{l+1}_{2i,2j+1} + \phi^{l+1}_{2i+1,2j+1}\right), \tag{4.1}$$

see the left drawing of Figure 4. The projection operator is exact and unique. On the other hand, to estimate the cell average at a level $l+1$ from those at the next coarser level l, we define a *prediction operator* (see the right drawing of Figure 4) $\mathrm{P}_{l\to l+1} : \phi^l \to \hat{\phi}^{l+1}$. This prediction operator must satisfy $\mathrm{P}_{l+1\to l} \circ \mathrm{P}_{l\to l+1} = \mathrm{Id}$, and is not unique. We employ the following standard polynomial interpolant:

$$\begin{aligned}
\hat{\phi}^{l+1}_{2i,2j} &= \phi^l_{ij} - Q^s_x\big(i,j,\phi^l\big) - Q^s_y\big(i,j,\phi^l\big) + Q^s_{xy}\left(i,j,\phi^l\right),\\
\hat{\phi}^{l+1}_{2i+1,2j} &= \phi^l_{ij} + Q^s_x\big(i,j,\phi^l\big) - Q^s_y\big(i,j,\phi^l\big) - Q^s_{xy}\big(i,j,\phi^l\big),\\
\hat{\phi}^{l+1}_{2i,2j+1} &= \phi^l_{ij} - Q^s_x\big(i,j,\phi^l\big) + Q^s_y\big(i,j,\phi^l\big) - Q^s_{xy}\big(i,j,\phi^l\big),\\
\hat{\phi}^{l+1}_{2i+1,2j+1} &= \phi^l_{ij} + Q^s_x\big(i,j,\phi^l\big) + Q^s_y\big(i,j,\phi^l\big) + Q^s_{xy}\big(i,j,\phi^l\big),
\end{aligned}$$

where the terms Q^s_x, Q^s_y and Q^s_{xy} are given by the respective expressions

$$Q^s_x\big(i,j,\phi^l\big) = \sum_{p=1}^{s} \gamma_p\big(\phi^l_{i+p,j} - \phi^l_{i-p,j}\big), \quad Q^s_y\big(i,j,\phi^l\big) = \sum_{q=1}^{s} \gamma_q\big(\phi^l_{i,j+q} - \phi^l_{i,j-q}\big),$$

$$Q^s_{xy}\big(i,j,\phi^l\big) = \sum_{p=1}^{s} \gamma_p \sum_{q=1}^{s} \gamma_q\big(\phi^l_{i+p,j+q} - \phi^l_{i+p,j-q} - \phi^l_{i-p,j+q} + \phi^l_{i-p,j-q}\big),$$

where s is the number of nearest uncles required for the interpolation, and the order of the approximation is $r = 2s - 1$. The corresponding coefficients γ_p are given by

$$\gamma_1 = -\frac{1}{8} \quad \text{for } s = 1, \qquad \gamma_1 = -\frac{22}{128}, \quad \gamma_2 = -\frac{3}{128} \quad \text{for } s = 2.$$

The difference $d^l_{ij} := \phi^l_{ij} - \hat{\phi}^l_{ij}$ between the exact and the predicted cell average value is called *detail*. These details are small in zones where the solution is smooth. Thus, if a detail d^l_{ij} is small in absolute value compared with a level-dependent threshold value ε_l, then the mesh can be coarsened near the corresponding position, i.e., leaves are removed from the tree. The MR transform $\mathbf{M}$ and its inverse $\mathbf{M}^{-1}$ are defined in Algorithms 4.1 and 4.2, respectively.

Algorithm 4.1 (Multiresolution transform $\mathbf{M}$).

```
Input: $\phi^L_{ij}$ for $i,j = 1,\dots,2^L - 1$
do $l = L-1, L-2, \dots, 0$
    do $i = 0,\dots,2^l - 1$
        do $j = 0,\dots,2^l - 1$
            $\phi^l_{ij} \leftarrow \frac{1}{4}\big(\phi^{l+1}_{2i,2j} + \phi^{l+1}_{2i+1,2j} + \phi^{l+1}_{2i,2j+1} + \phi^{l+1}_{2i+1,2j+1}\big)$
        enddo
    enddo
    do $i = 0,\dots,2^l - 1$
        do $j = 0,\dots,2^l - 1$
            $d^{l+1}_{ij} \leftarrow \phi^{l+1}_{ij} - \hat{\phi}^{l+1}_{ij}$
        enddo
    enddo
enddo
Output: $d^l_{ij}$ and $\phi^l_{ij}$ for $i,j = 1,\dots,2^l - 1$ and $l = 0,\dots,L$
```

Algorithm 4.2 (Inverse multiresolution transform $\mathbf{M}^{-1}$).

```
Input: $\phi^0_{0,0}$ and $d^l_{ij}$ for $i,j = 1,\dots,2^l - 1$ and $l = 1,\dots,L$
do $l = 1,\dots,L$
    do $i = 0,\dots,2^l - 1$
        do $j = 0,\dots,2^l - 1$
            $\phi^l_{ij} \leftarrow d^l_{ij} + \hat{\phi}^l_{ij}$
        enddo
    enddo
enddo
```

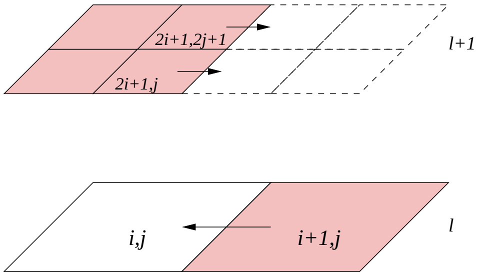

FIGURE 5. Enforcing the conservativity of the flux computation between cells lying on different resolution levels.

Output: ϕ^l_{ij} *for* $i,j=1,\dots,2^l-1$ *and* $l=0,\dots,L$

4.3. Conservative flux evaluation and boundary conditions. The main idea behind MR schemes is to only use the costly flux evaluations at locations where the solution exhibits steep gradients or near discontinuities. Then, the numerical scheme will become more efficient by eliminating flux computations wherever the solution is smooth. In this respect, in the graded tree we must guarantee conservativity of the numerical scheme when computing numerical fluxes on different levels [52]. We employ the following rule illustrated in Figure 5. We compute only the fluxes at level $l+1$, considering that

$$\mathrm{F}^l_{(i+1,j)\to(i,j)} = \frac{1}{2}\left(\mathrm{F}^{l+1}_{(2i+1,2j)\to(2i+2,2j)} + \mathrm{F}^{l+1}_{(2i+1,2j+1)\to(2i+2,2j+1)}\right).$$

Another important point here is to impose the boundary condition at each level of the tree. Figure 6 illustrates that this involves the definition of uncles outside of the domain at each level, called “virtual uncles”.

4.4. Error analysis and thresholding for the conservation law. Following [21, 52], we consider the cell average values of the exact solution at level L, denoted by ϕ^L_{e}, the approximate solution at level L using the FV scheme denoted by ϕ^L_{FV}, and the solution obtained from the MR scheme, denoted ϕ^L_{MR}. Then we can write

$$\left\|\phi^L_{\mathrm{e}} - \phi^L_{\mathrm{MR}}\right\| \leq \left\|\phi^L_{\mathrm{e}} - \phi^L_{\mathrm{FV}}\right\| + \left\|\phi^L_{\mathrm{FV}} - \phi^L_{\mathrm{MR}}\right\|.$$

The first and second term on the right-hand side are the discretization and perturbation errors, respectively. The first term can be bounded as follows:

$$\left\|\phi^L_{\mathrm{e}} - \phi^L_{\mathrm{FV}}\right\| \leq C2^{-\alpha L}, \quad C>0,$$

where α is the order of convergence of the FV scheme, which is assumed to be known here. In our case $\alpha \leq 2$. For the second term, the perturbation error, we assume for the hyperbolic case, as proposed in [21], that $\varepsilon_l = 2^{2(l-L)}\varepsilon_{\mathrm{ref}}$, where l is the corresponding level and $\varepsilon_{\mathrm{ref}}$ is a reference tolerance. Now we have

$$\left\|\phi^L_{\mathrm{e}} - \phi^L_{\mathrm{MR}}\right\| \leq Cn\varepsilon, \quad C>0$$

where n is the number of time steps. In the numerical computations, we take the reference tolerance $\varepsilon_{\mathrm{ref}} = 2^{-(\alpha+1)L}\Delta t C$. Then, the thresholding operator consists in removing the nodes in the tree structure whose *detail* is smaller in absolute value than the level-dependent tolerance ε_l.

5. Numerical approximation of the Stokes system

The discretization of (2.2), (2.3) is based on the pressure stabilization framework discussed in Section 2. Our formulation follows the development presented by Eymard et al. [26], where the authors propose a FV scheme for the Stokes system (in the case of constant viscosity). We herein extend their method to a variable viscosity $\mu = \mu(\phi)$. As usual, the unknowns are the velocity $\mathbf{v}$ of the flow and the pressure p in each control volume $\Omega_{ij}^L \in \mathcal{T}^L$ (the finest mesh, where L denotes the finest level). To clarify the notation we denote a generic control volume by $K = \Omega_{ij}^L$, $\sigma = K|K^*$ is the common boundary between two neighbors K and K^*, ξ is the set of all edges, m_σ is the size of the boundary, $d_{K,K^*} = |x_{K^*} - x_K|$, $\tau_\sigma = m_\sigma/d_\sigma$, and $\mathbf{n}_{K,\sigma}$ stands for the outward unit vector of the edge σ of K. The set of edges of K is denoted by ξ_K, and the sets of interior and boundary edges are denoted by ξ_{int} and ξ_{ext}, respectively, that is, $\xi_{\text{int}} = \{\sigma \in \xi \,|\, \sigma \notin \partial\Omega\}$ and $\xi_{\text{ext}} = \{\sigma \in \xi \,|\, \sigma \subset \partial\Omega\}$. For the FV scheme with the properties above, let $\mathcal{T}(= \mathcal{T}^L)$ be an admissible discretization of Ω in the sense of [25]. By $H_{\mathcal{T}}(\Omega) \subset L^2(\Omega)$ we denote the space of functions which are piecewise constant on each control volume.

The regularized Stokes problem (2.4) is approximated as follows. We seek functions $\mathbf{v} \in E_{\mathcal{T}}(\Omega)$, $p \in H_{\mathcal{T}}(\Omega)$ with $\int_\Omega p(\mathbf{x})\,\mathrm{d}\mathbf{x} = 0$ such that

$$(5.1) \qquad [\mathbf{v},\mathbf{u}]_{\mathcal{T},\mu} - \lambda \int_\Omega p(\mathbf{x})\operatorname{div}_{\mathcal{T}}\mathbf{u}(\mathbf{x})\,\mathrm{d}\mathbf{x} = \int_\Omega \mathbf{f}(\mathbf{x}) \cdot \mathbf{u}(\mathbf{x})\,\mathrm{d}\mathbf{x} \quad \forall \mathbf{u} \in H_{\mathcal{T}}(\Omega)^2,$$

where the index $\mathcal{T}$ indicates the discrete operators with respect to the mesh $\mathcal{T}$, and $[\cdot,\cdot]_{\mathcal{T},\mu}$ represents the weighted inner product defined by

$$[\mathbf{v},\mathbf{u}]_{\mathcal{T},\mu} := \langle \mathbf{v},\mathbf{u}\rangle_{\mathcal{T},\mu} + \sum_{K\in\mathcal{T}} \sum_{\sigma\in\xi_K\cap\xi_{ext}} \frac{m_\sigma}{d_{K,\sigma}} \mu_K \mathbf{v}_K \cdot \mathbf{u}_K,$$

where $\mu_K := \mu(\phi_K) = (1-\phi_K)^{-\beta}$ for all $K \in \mathcal{T}$ and

$$\langle \mathbf{v},\mathbf{u}\rangle_{\mathcal{T},\mu} := \frac{1}{2} \sum_{K\in\mathcal{T}} \sum_{K^*\in N_K} \frac{m_{K|K^*}}{d_{K,K^*}(\mu_K + \mu_{K^*})} (\mathbf{v}_{K^*} - \mathbf{v}_K) \cdot (\mathbf{u}_{K^*} - \mathbf{u}_K).$$

Since we use a collocated approximation for the velocity and pressure fields, the scheme has to be stabilized to avoid spurious oscillations in the pressure field. Using the Brezzi-Pitkäranta stabilization [9], we then look for $(\mathbf{v},p) \in H_{\mathcal{T}}(\Omega)^2 \times H_{\mathcal{T}}(\Omega)$ with $\int_\Omega p(\mathbf{x})\,\mathrm{d}\mathbf{x} = 0$ such that (5.1) holds along with

$$(5.2) \qquad \int_\Omega \operatorname{div}_{\mathcal{T}}\mathbf{v}(\mathbf{x}) q(\mathbf{x})\,\mathrm{d}\mathbf{x} = -\eta^2 \langle p,q\rangle_{\mathcal{T}} \quad \forall q \in H_{\mathcal{T}}(\Omega).$$

Here, $0 < \eta \leq 1$ is an adjustable parameter of the discrete formulation which must be tuned to achieve a satisfactory balance between accuracy and stability, and we define

$$\langle p,q\rangle_{\mathcal{T}} := \frac{1}{2} \sum_{K\in\mathcal{T}} \sum_{K^*\in N_K} \frac{m_{K|K^*}}{d_{K,K^*}} (p_{K^*} - p_K)(q_{K^*} - q_K).$$

The system (2.4) is approximated by the following scheme, which arises from integrating relations (2.4) over each control volume $K \in \mathcal{T}$:

$$\forall K \in \mathcal{T}: \qquad \sum_{\sigma\in\xi_K} \mathbf{F}_{K,\sigma} + \lambda \sum_{\sigma\in\xi_K\cap\xi_{\text{int}}} \mathbf{A}_{K,\sigma}(p_{K^*} - p_K) = \mathbf{f}_K,$$

$$\sum_{\sigma\in\xi_K\cap\xi_{\text{int}}} \mathbf{A}_{K,\sigma} \cdot (\mathbf{v}_K + \mathbf{v}_{K^*}) - \eta^2 \sum_{\sigma\in\xi_K\cap\xi_{\text{int}}} \tau_\sigma (p_{K^*} - p_K) = 0,$$

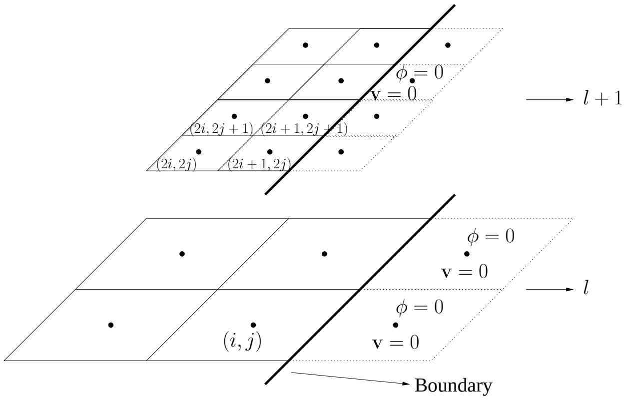

FIGURE 6. Sketch of virtual uncles outside of the domain, needed for the flux computation of boundary nodes.

where $\sigma = K|K^*$, and we define

$$\mathbf{A}_{K,\sigma} := \frac{1}{2} m_\sigma \mathbf{n}_{K,\sigma} \quad \forall K \in \mathcal{T}, \sigma \in \xi_K,$$

and assume that

$$\mathbf{F}_{K,\sigma} \approx - \int_\sigma \mu_K \nabla \mathbf{v}(\mathbf{x}) \cdot \mathbf{n}_{K,\sigma} \, \mathrm{d}\gamma.$$

To ensure that the scheme is conservative, we define for all $K \in \mathcal{T}$

$$\mathbf{F}_{K,\sigma} := \begin{cases} m_\sigma \dfrac{\mu_K \mu_{K^*}}{\mu_K d_{K,\sigma} + \mu_{K^*} d_{K^*,\sigma}} (\mathbf{v}_K - \mathbf{v}_{K^*}) & \text{if } \sigma = K|K^* \in \xi_{\text{int}}, \\ m_\sigma \dfrac{\mu_K}{d_{K,\sigma}} \mathbf{v}_K & \text{if } \sigma \in \xi_{\text{ext}}. \end{cases}$$

To summarize the scheme, we define the bilinear forms

$$T(\mathbf{v}, \mathbf{u}) := [\mathbf{v}, \mathbf{u}]_{\mathcal{T},\mu}, \quad S(p, q) := \langle p, q \rangle_{\mathcal{T}}, \quad R(\mathbf{u}, p) := \lambda \int_\Omega p(\mathbf{x}) \mathrm{div}_{\mathcal{T}} \mathbf{u}(\mathbf{x}) \, \mathrm{d}\mathbf{x}.$$

Then the problem is to find $(\mathbf{v}, p) \in E_{\mathcal{T}}(\Omega) \times H_{\mathcal{T}}(\Omega)$ such that

$$\begin{aligned} \forall (\mathbf{u}, q) \in H_{\mathcal{T}}(\Omega)^2 \times H_{\mathcal{T}}(\Omega): \qquad T(\mathbf{v}, \mathbf{u}) - R(\mathbf{u}, p) &= G(\mathbf{u}), \\ R(\mathbf{v}, q) + \eta_*^2 S(p, q) &= 0. \end{aligned}$$

This can equivalently be stated as follows: find $(\mathbf{v}, p) \in E_{\mathcal{T}}(\Omega) \times H_{\mathcal{T}}(\Omega)$ such that

$$\begin{bmatrix} T & -R \\ R^* & \eta_*^2 S \end{bmatrix} \begin{pmatrix} \mathbf{u} \\ p \end{pmatrix} = \begin{pmatrix} G \\ 0 \end{pmatrix},$$

where the matrix is symmetric if we take the stabilization term as $\eta^2 = \eta_*^2/\lambda$.

6. Coupling strategy and algorithm description

6.1. Some general remarks. So far we have presented discretization strategies for the two sub-problems involved in the whole system. In this section we discuss our choice for the coupling procedure. Firstly, for the FV formulation of the coupled system (2.1), (2.2) and (2.3) on an admissible mesh (in the sense of Definition 3.1), the coupling follows a fully segregated approach, i.e.,

(a) The initial datum for the concentration $\phi(0) = \phi_0$ is specified.
(b) Knowing the concentration field at time t, the Stokes system is solved.

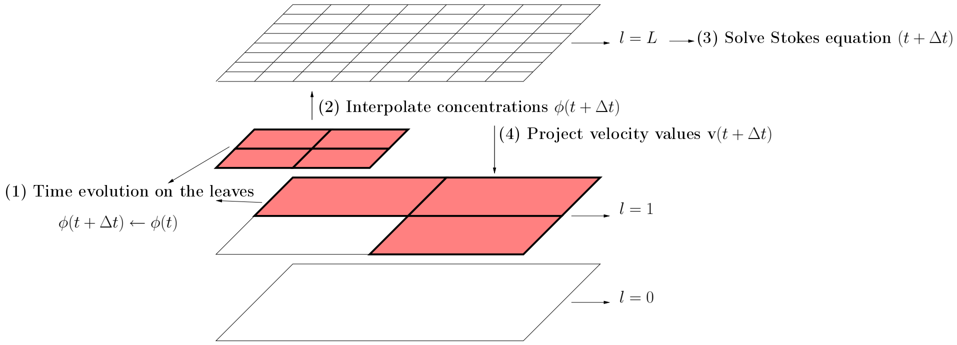

FIGURE 7. Sketch of the coupling strategy used at the discrete level.

(c) Knowing concentration, velocity, and pressure fields at time t, we solve the hyperbolic equation for the concentration at the next time step $t + \Delta t$.

(d) We replace the concentracion $\phi(t)$ by $\phi(t+\Delta t)$. We set $t = t + \Delta t$, and repeat steps (b) to (d) until the final time is reached.

Regarding the coupling algorithm for the method using MR, we perform a MR analysis for the concentration field only. This obeys mainly to our interest in capturing sharp fronts of the concentration. The flow fields are solved using a pure FV formulation on the finest resolution level L, which implies that there is no compression at this stage. Once this step is achieved, we utilize the projection operator (4.1) for the values of the velocity, and send this information to all leaves in the current graded tree to perform the evolution in time. Once the evolution time is done, we use the prediction operator to transfer the information related to the concentration field to the finest mesh, where the Stokes problem will be solved, see Figure 7.

6.2. Description of the algorithm. We first describe the subroutine of *remeshing* the tree, remembering that Λ is the set of indices of the existing nodes, $\mathcal{L}(\Lambda)$ is the set of indices of the leaves, and Λ_l contains the indices of a particular level l. We denote by Λ_{del} the set of the deletable nodes.

Algorithm 6.1 (Remeshing).
Recalculate values in nodes and detail using the transform $\mathbf{M}$ *restricted to* Λ.

```
do $l = L-1, L-2, \dots, 0$
    do $(i,j,l) \in \Lambda_l$
        if $\max\{|d^{l+1}_{2i,2j}|, |d^{l+1}_{2i+1,2j}|, |d^{l+1}_{2i,2j+1}|, |d^{l+1}_{2i+1,2j+1}|\} < \varepsilon_{l+1}$ then
            $\Lambda_{\mathrm{del}} \leftarrow \Lambda_{\mathrm{del}} \cup \{(2i+p, 2j+q, l+1) \,|\, p,q = 0,1\}$
        endif
    enddo
enddo
do $l = L-1, L-2, \dots, 0$
    do $(i,j,l) \in \Lambda_l$
        if $(i,j,l) \in \Lambda_{\mathrm{del}}$ and $(2i,2j,l+1) \in \Lambda_{\mathrm{del}}$ and $(2i,2j,l+1) \in \mathcal{L}(\Lambda)$
        then
            $\Lambda \leftarrow \Lambda \backslash \{(2i+p, 2j+q, l+1) \,|\, p,q = 0,1\}$
```

```
                endif
                if $(i,j,l) \notin \Lambda_{\mathrm{del}}$ and $l < L$ then
                    $\Lambda \leftarrow \Lambda \cup \{(2i+p, 2j+q, l+1) \,|\, p,q = 0,1\}$
                endif
            enddo
        enddo
```

Algorithm 6.2 (Coupled system)**.**

```
(1) Initialize:
        Initialize data: final time, domain dimensions, $C$, $L$, $\eta^2$, initial concentration $\phi(0)$, etc.
        Calculate $\mathbf{v}(0)$, $p(0)$, solving the Stokes system (2.2) with $\phi(0)$.
        Create the initial tree: calculate the root cell average $\phi^0_{0,0}$.
        do $l = 1, \dots, L$
            do $(i,j,l) \in \Lambda_l$
                Calculate cell average $\phi^l_{ij}$ and $d^l_{ij}$.
                if $|d^l_{ij}| > \varepsilon^l$ then
                    $\Lambda \leftarrow \Lambda \cup \{(2i+p, 2j+q, l+1) \,|\, p,q = 0,1\}$
                else
                    $\mathcal{L}(\Lambda_l) \leftarrow \mathcal{L}(\Lambda_l) \cup \{(i,j,l)\}$
                endif
            enddo
        enddo
        Send $\mathbf{v}(0)$ to the leaves in the tree by projection operator.
        $t \leftarrow 0$
(2) Iterate in time:
        while $t < T$ do
            Calculate (3.3) $\Delta t^L$ (last level) satisfying CFL condition.
            Time evolution:
                Solve (3.1). Compute $\phi(t + \Delta t^L/2)$ for all the leaves.
                Solve (3.2). Compute $\phi(t + \Delta t^L)$ for all the leaves.
            Send $\phi(t + \Delta^L)$ to the finest level $L$ the predictor operator.
            Solve (2.2). Compute $\mathbf{v}(t+\Delta^L)$, $p(t+\Delta^L)$ on the finest level $L$.
            Send $\mathbf{v}(t + \Delta t^L)$ to the leaves in the tree by projection operator.
            Remesh (Algorithm 6.1).
            $t \leftarrow t + \Delta t^L$
        endwhile
```

7. Numerical Examples

We now present some tests to illustrate the properties of our numerical scheme. We first perform a detailed study on the uncoupled subproblem for the concentration field, and then we discuss results obtained for the fully coupled problem.

7.1. Example 1 and 2: hyperbolic problem.

In this subsection we want to analyze different properties of our MR method, such as convergence, speedup and accuracy. To this end, we start by considering an uncoupled problem consisting only of the hyperbolic conservation law. The data compression rate [5]

$$\omega := 4^L / \big(1 + |\mathcal{L}(\Lambda)|\big)$$

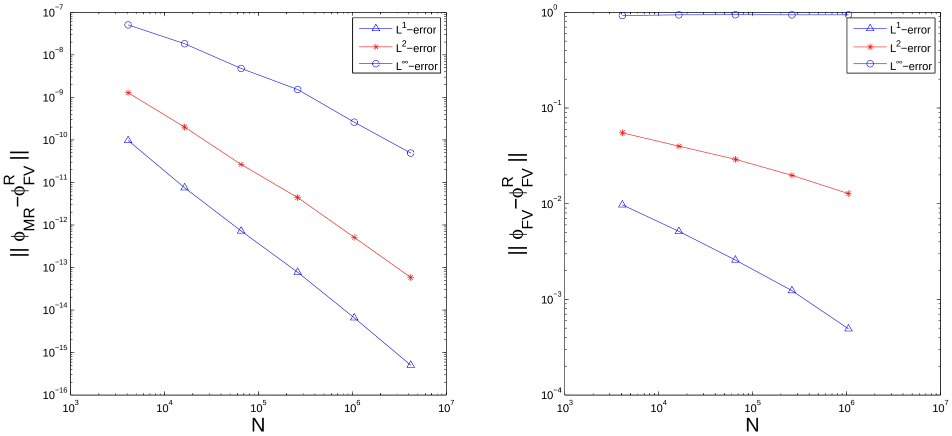

FIGURE 8. Example 1 (hyperbolic problem): errors between the reference and the MR solutions (left) and between the reference and FV solutions (right) for different finest resolution levels$L$.

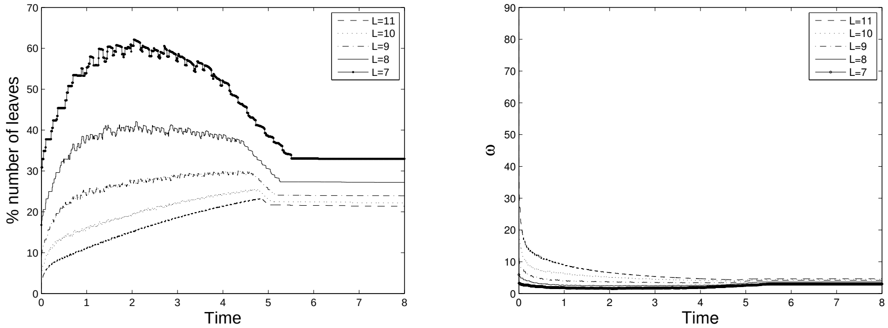

FIGURE 9. Example 1 (hyperbolic problem): evolution of the percentage of number of leaves for different resolution levels L, for $C = 0.1$ (left). Data compression rate (right). Time between $t = 0$ and $t = T = 8$.

is used to measure the possible improvement in data compression, where $|\mathcal{L}(\Lambda)|$ is the total number of leaves. The speedup between the CPU times of the numerical solutions obtained by the FV method in the last level and MR method is given by

$$\zeta := (\mathrm{CPUtime})_{\mathrm{FV}}/(\mathrm{CPUtime})_{\mathrm{MR}},$$

where the CPU time measured for the MR scheme includes the total number of operations for the adaptive method (of refreshing the tree, deleting and creating leaves, etc.).

In Example 1, let us consider a channel of height $2x_h = 10$, with an inclination angle of $\theta = 30°$ with respect to gravity, and an initial condition given by $\phi_0 = 0.2$. The velocity field is taken equal to zero in the whole channel. We start by giving the convergence history, where in absence of a closed-form exact solution a FV solution computed on a uniformly refined mesh is used as reference ($L = 11$). For the MR

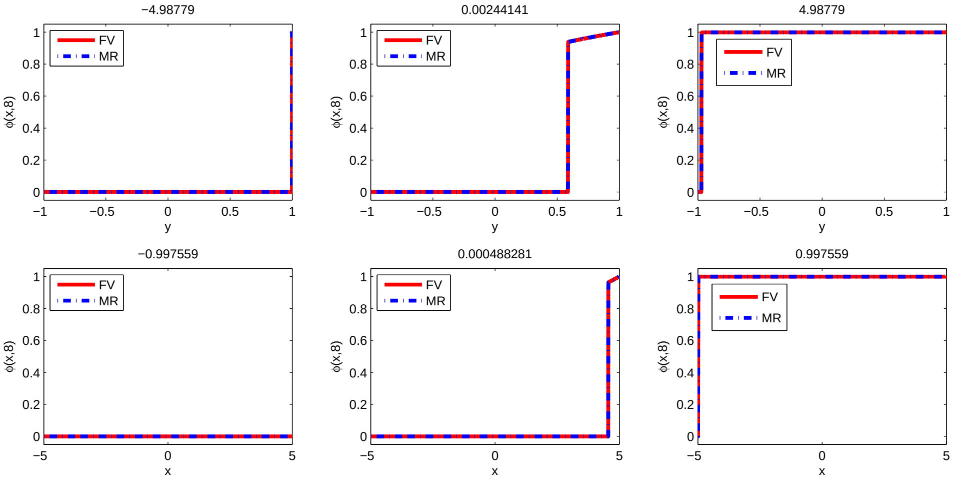

Figure 10. Example 1 (hyperbolic problem): Horizontal cuts (top) in the channel at $y = -0.9975$ (left), $y = 0.00048$ (middle) and $y = 0.9975$ (right). Vertical cuts (bottom) in the channel at $x = -4.9877$ (left), $x = 0.002441$ (middle) and $x = 4.9877$ (right).

setting, we recall the thresholding tolerance given by

$$\varepsilon_l = C\Delta t 2^{2(l-L)}. \tag{7.1}$$

Figure 8 shows errors in L^1, L^2 and L^∞ norms for both FV and MR computations using $C = 0.1$. Here, for the MR solution we use the values on the each finest level L obtained by prediction from the corresponding leaf. The right plot of Figure 8 show that the L^1 and L^2 orders of the FV scheme are between 1/2 and 1. On the other hand, the scheme does not converge in L^∞, which is a well-known property of approximations to discontinuous solutions. The left plot of Figure 8 illustrates that the thresholding error decays faster (with order between 1 and 2) than the error of the FV scheme. Thus, the adaptive scheme preserves the accuracy of the FV scheme.

In Figure 9 the time evolution of the percentage of the number of leaves of the graded tree (nodes which are actually used in the flux computation) with respect to the total number of nodes and the data compression rate ω. In Figure 10 we display vertical and horizontal profiles, for the comparison of the respective MR and reference solutions with $L = 11$. Figure 11 displays the corresponding MR solution at time $t = 8$. (In this and following figures, numerical solutions on Ω are plotted inclined applying the true angle of inclination θ.) The sediment region, with values of ϕ close to one, does not feature constant concentration; rather, concentration gradually increases towards the wall $y = 1$, similarly to the top middle plot of Figure 10. This slow variation causes refinement in the sediment region.

For illustration, we consider in Example 2 the discontinuous initial condition

$$\phi_0 = \begin{cases} 0.0 & \text{if } -x_h \le x \le -x_h - (y-1)\tan\theta, \\ 0.3 & \text{if } -x_h - (y-1)\tan\theta < x < x_h - (y+1)\tan\theta, \\ 0.6 & \text{if } x_h - (y+1)\tan\theta \le x \le x_h, \end{cases}$$

with an angle of inclination $\theta = 30°$. Figure 12 shows the CPU time speedup and memory compression at time $t = 0.1$. For increasing L we observe that both the

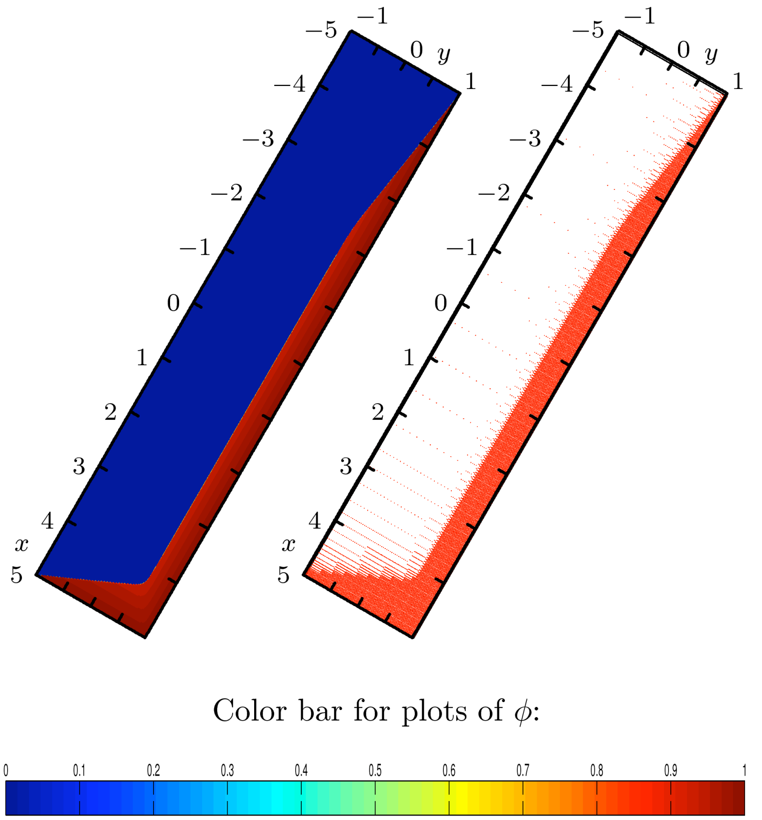

FIGURE 11. Example 1 (hyperbolic problem): numerical solution for the concentration ϕ (left) and leaves of the tree data structure (right) at $t = 8$.

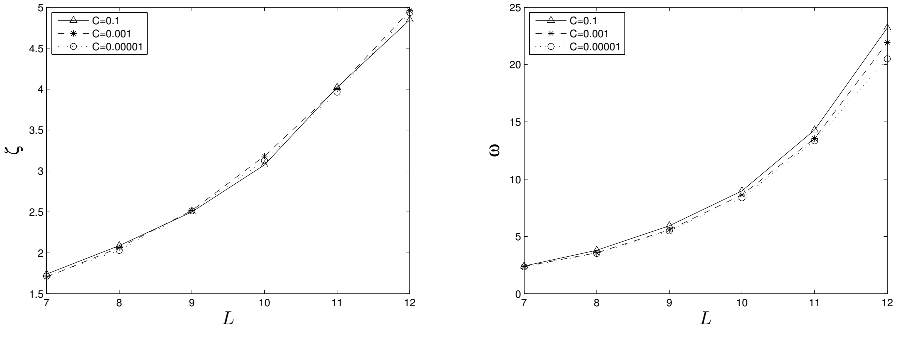

FIGURE 12. Example 2 (hyperbolic problem): CPU time speedup ζ (left) and memory compression ω (right) for different values of L and C at time $t = 0.1$.

data and CPU time compression increase, which shows that the adaptive scheme becomes more efficient than the FV method.

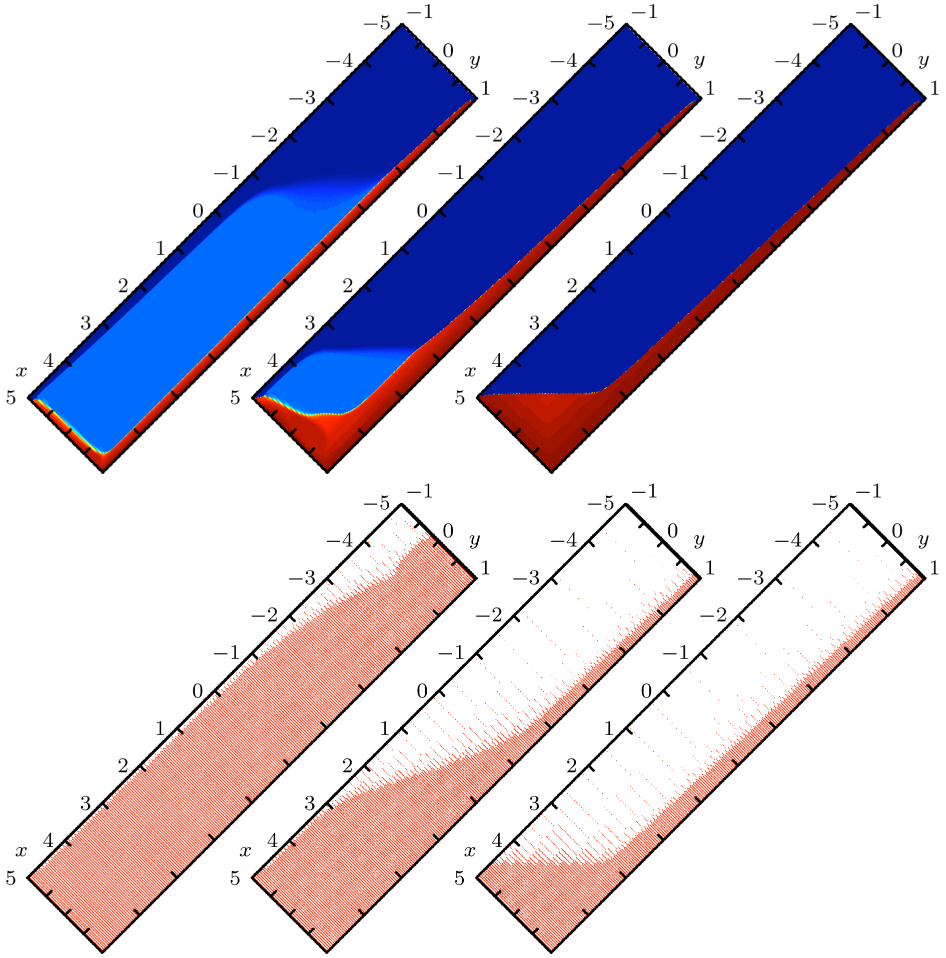

FIGURE 13. Example 3 (coupled problem, $\theta = 45°$, $L = 8$, $\eta^2 = 1/9000$): numerical solution for the concentration ϕ (top) and leaves of the tree (bottom) at times $t = 1.5$ (left), $t = 3.75$ (middle), and $t = 11.25$ (right).

7.2. Examples 3–6: coupled system. In this section we present our numerical results obtained for the whole coupled flow and transport problem. For the Stokes and concentration equations, the following geometrical and physical parameters will be considered: $B = 0.67$, $x_h = 5$, $n_{\mathrm{RZ}} = 2$, and $\beta = 2$. For our MR method we will also consider a thresholding tolerance given by (7.1), where we will vary the maximum resolution level L. Examples 3, 4, and 5 have the same data, differing only in the stabilization parameter η. In Example 3 we consider an inclination of the channel of $\theta = 45°$, while the initial condition is given by a constant distribution over the whole channel $\phi_0 = 0.2$. For the MR procedure, we will consider $L = 8$ resolution levels. Figure 13 shows the evolution in time of the concentration field and of the leaves of the graded tree, and Figure 14 displays the corresponding pressure fields and flow velocities, for times $t = 1.5$, $t = 3.75$ and $t = 11.25$. Note that we have applied available plot routines for the snapshots of velocity fields in Figure 14 and following figures so that arrows do not intersect. The arrows

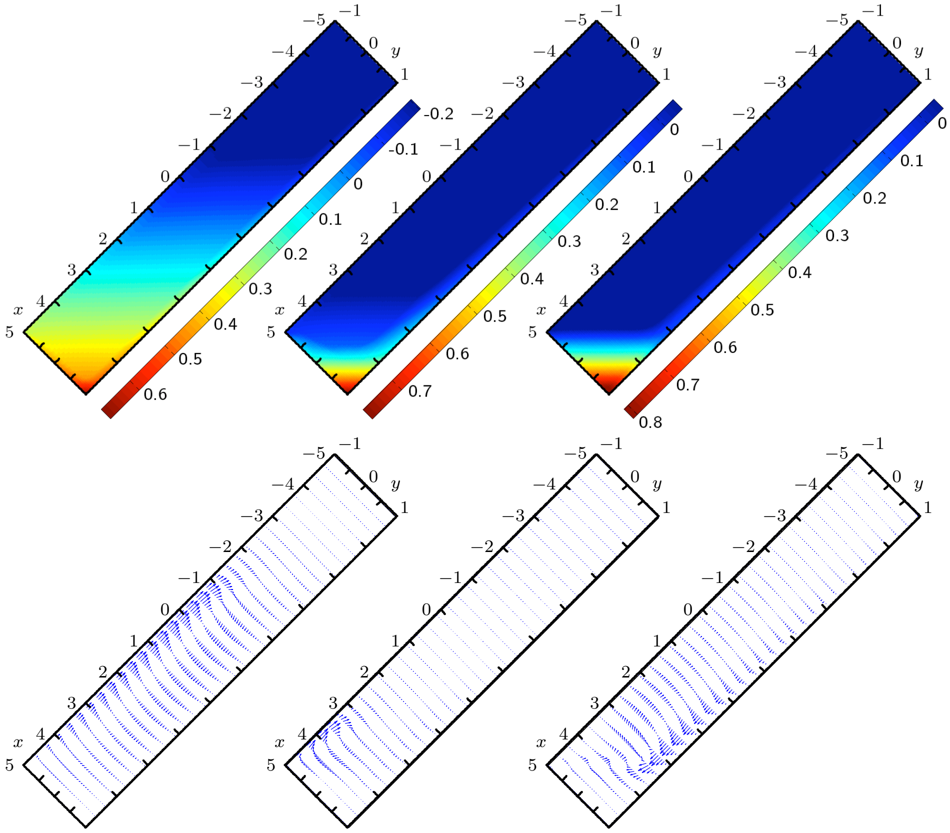

FIGURE 14. Example 3 (coupled problem, $\theta = 45°$, $L = 8$, $\eta^2 = 1/9000$): numerical solution for the pressure p (top) and the velocity $\mathbf{v}$ (bottom) at times $t = 1.5$ (left), $t = 3.75$ (middle), and $t = 11.25$ (right), with $\|\mathbf{v}(1.5)\| = 11.84$, $\|\mathbf{v}(3.75)\| = 3.72$ and $\|\mathbf{v}(11.25)\| = 2.7 \times 10^{-2}$.

correspond to values of $\mathbf{v}$ on a 32×32 grid on Ω that have been averaged from the values $\{\mathbf{v}_K(t)\}_{K\in\mathcal{T}}$ obtained on the full 256×256 mesh $\mathcal{T}$ (corresponding to $L = 8$) at the corresponding time t. In each plot the longest arrow has the approximate length $\|\mathbf{v}(t)\| := \max_{K\in\mathcal{T}} \|\mathbf{v}_K(t)\|_2$; this value is indicated for each velocity plot appearing in this and the following figures.

In Figures 13 and 14, we observe a clear phase separation, and that the concentration exhibits strong gradients between the sediment and the suspension zones. For the stabilization of the numerical solution of the Stokes problem, first we take the parameter $\eta^2 = 1/9000$ and for the thresholding operation we consider $C = 0.001$.

Furthermore, we wish to analyze the effect of the stabilization parameter η. To this end, we choose in Examples 4 and 5 the initial datum and θ as in Example 3, but choose $\eta^2 = 1/90$ and $\eta^2 = 1/90000$, respectively. Figure 15 shows the numerical solutions for ϕ, p and $\mathbf{v}$ obtained in each of these cases at times $t = 3.75$ and $t = 11.25$ We have found that the value $\eta^2 = 1/9000$ (corresponding to the results shown in Figures 13 and 14) will in general produce a good compromise between accuracy and avoidance of oscillations in p. The solutions presented for alternative

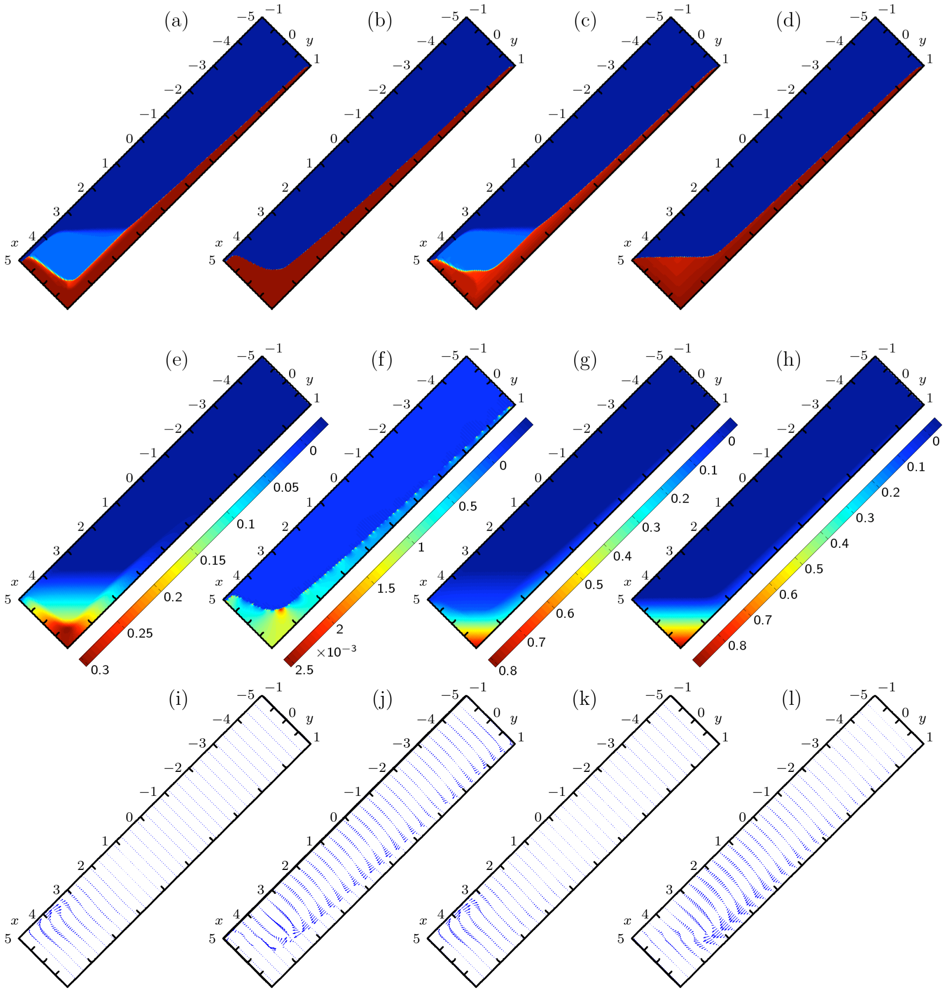

FIGURE 15. Examples 4 and 5 (coupled problem, $\theta = 45°$, $L = 8$): numerical solution for the concentration ϕ (top), the pressure p (middle) and the velocity $\mathbf{v}$ (bottom) for $\eta^2 = 1/90$ (Example 4, first and second column) and $\eta^2 = 1/90000$ (Example 5, third and fourth column) at times $t = 3.75$ (first and third column) and $t = 11.25$ (second and fourth column), with (i) $\|\mathbf{v}(3.75)\| = 3.28$, (j) $\|\mathbf{v}(11.25)\| = 6.88 \times 10^{-3}$, (k) $\|\mathbf{v}(3.75)\| = 3.73$ and (l) $\|\mathbf{v}(11.25)\| = 2.26 \times 10^{-2}$.

values of η^2 differ significantly, and show that this parameter is very important and modifies the solution. For example, for the value of $\eta^2 = 1/90$ (see Figure 15 (j)) at time $t = 11.25$ the pressure is nearly flat (as expressed by the scale of the color bar for p), but the velocity field exhibits some distortions e.g. near $x = 3.5$, $y = 0.5$ that indicate an appreciable local violation of $\nabla \cdot \mathbf{v} = 0$.

Finally, in Example 6 we study the effect of the angle of inclination. To this end, we consider again the same setup as in Example 3, and plot the numerical

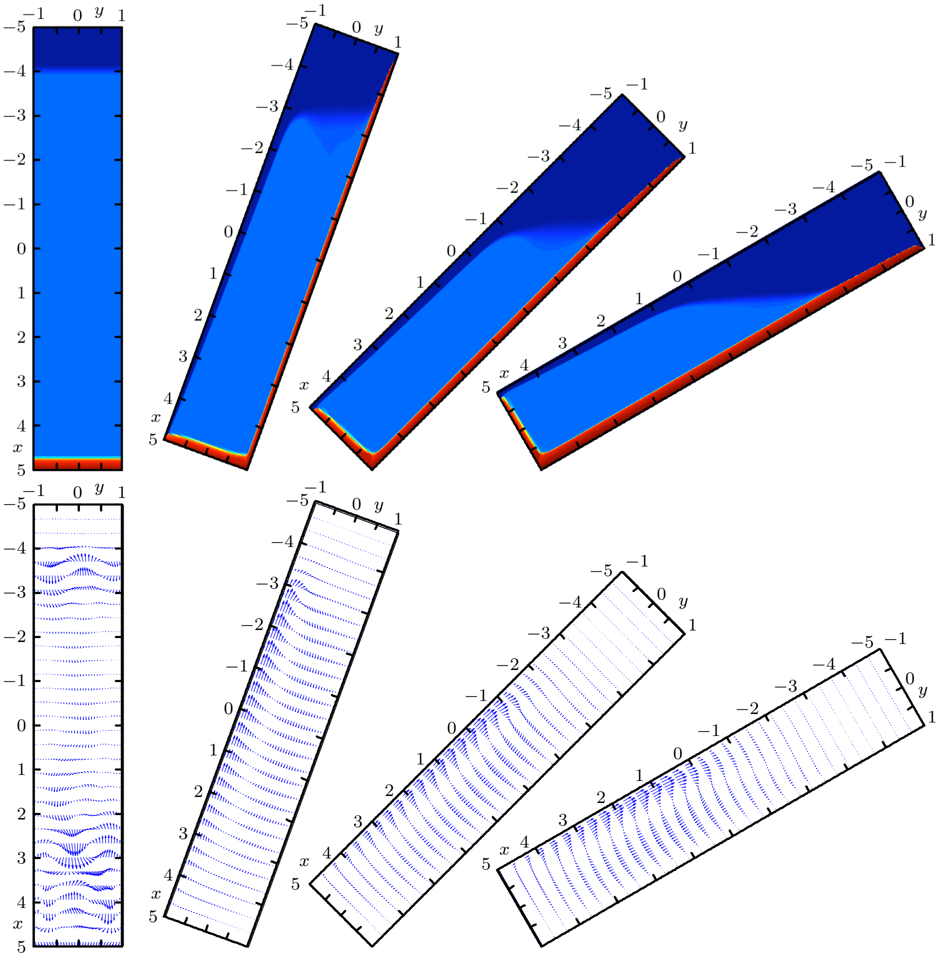

FIGURE 16. Example 6 (coupled problem, $L = 8$, $\eta^2 = 1/9000$): numerical solution for the concentration ϕ (top), and the velocity $\mathbf{v}$ (bottom) at time $t = 1.5$ for $\theta = 0°$, $\theta = 20°$, $\theta = 45°$, and $\theta = 60°$ (from left to right), with the respective values $\|\mathbf{v}(1.5)\| = 2.70 \times 10^{-4}$, 10.67, 11.84, and 9.47.

solution for ϕ and $\mathbf{v}$ simultaneously for $\theta = 0°$, $\theta = 20°$, $\theta = 45°$, and $\theta = 60°$ at four different times. We consider $C = 0.0001$. See Figures 16 to 19.

The numerical results confirm that the settling rate (understood as the rate of production of supernatant clear liquid) increases with θ. Moreover, we may compare the results for $\theta = 0°$ with those obtained from the one-dimensional kinematic sedimentation model by Kynch [35]. For batch settling of an initially homogeneous suspension of concentration ϕ_0 in a vertical column corresponding to $x \in [-x_h, x_h]$, this model reduces to the initial value problem

$$\frac{\partial \phi}{\partial t} + \frac{\partial f(\phi)}{\partial x} = 0, \quad \phi(x,0) = \begin{cases} 0 & \text{for } x < -x_h, \\ \phi_0 & \text{for } -x_h < x < x_h, \\ 1 & \text{for } x \geq x_h. \end{cases} \tag{7.2}$$

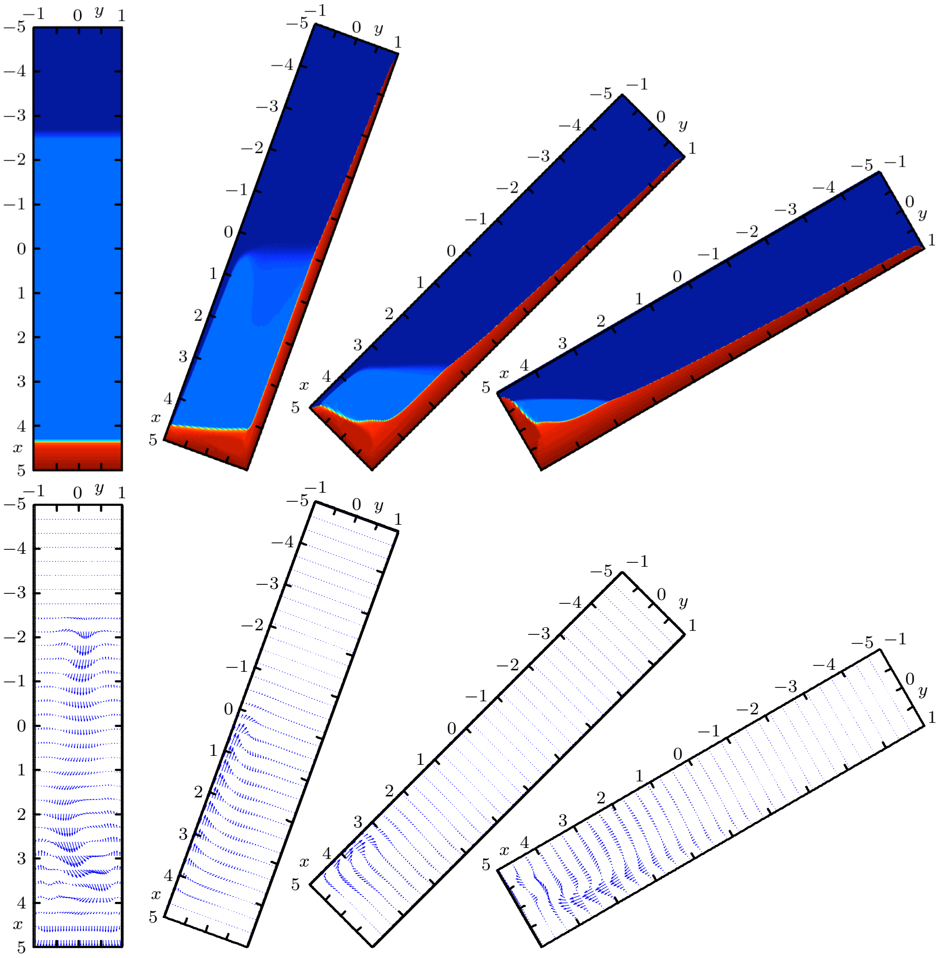

FIGURE 17. Example 6 (coupled problem, $L = 8$, $\eta^2 = 1/9000$): numerical solution for the concentration ϕ (top), and the velocity $\mathbf{v}$ (bottom) at time $t = 3.75$ for $\theta = 0°$, $\theta = 20°$, $\theta = 45°$, and $\theta = 60°$ (from left to right), with the respective values $\|\mathbf{v}(3.75)\| = 1.49 \times 10^{-4}$, 6.65, 3.72, and 0.5.

One feature of the (unique) entropy solution to this problem, which can be constructed explicitly [16, 18], consists in the fact that for $\phi_0 = 0.2$ and $n_{\mathrm{RZ}} = 2$, the suspension-supernate interface, initially located at $x = -x_h$, will travel downwards at the constant velocity σ given by the Rankine-Hugoniot condition $\sigma = (f(\phi_0) - f(0))/\phi_0 = (1 - \phi_0)^{n_{\mathrm{RZ}}} = 0.8^2 = 0.64$. Thus, at time t, and before the sediment level is reached, this interface should be located at position $x = -x_h + \sigma t$. For $-x_h = -5$ and $t = 1.5$, $t = 3.75$ and $t = 11.25$, we obtain the interface positions $x = -4.04$, $x = -2.6$ and $x = 2.2$, respectively, which are in excellent agreement with the (albeit slightly blurred) interface positions observed in the concentration plots for $\theta = 0°$ of Figures 16, 17 and 18, respectively.

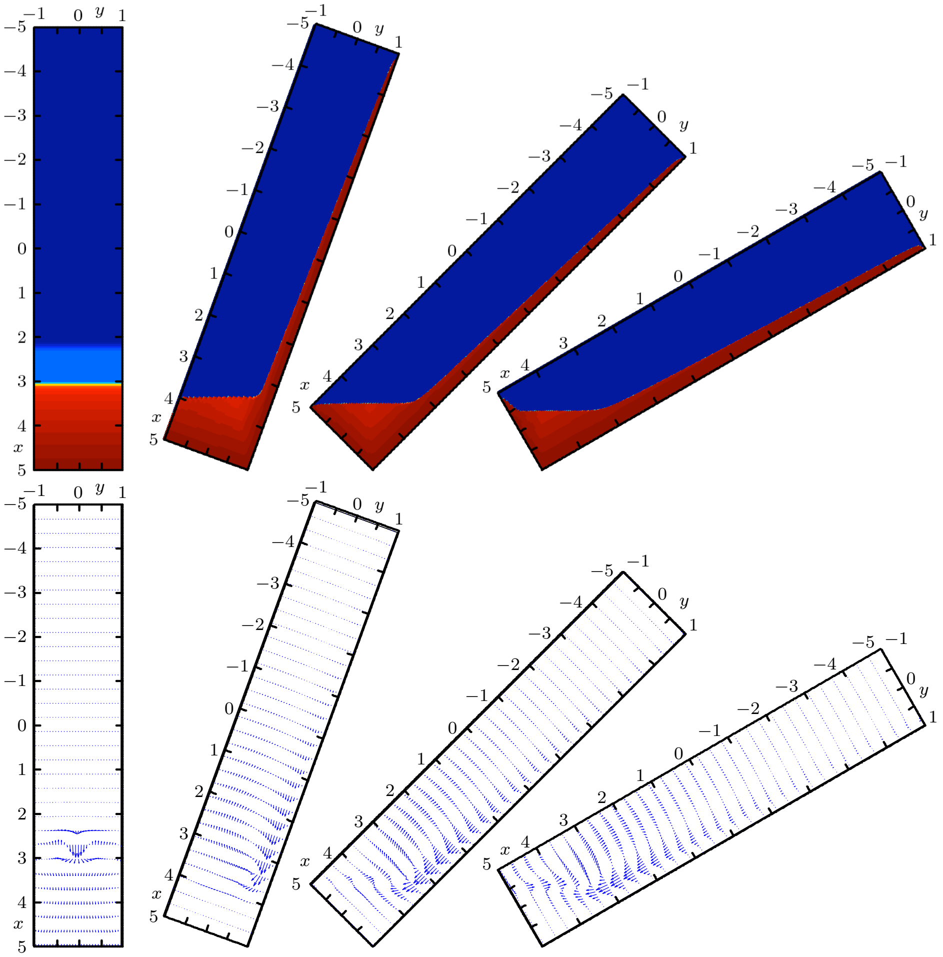

FIGURE 18. Example 6 (coupled problem, $L = 8$, $\eta^2 = 1/9000$): numerical solution for the concentration ϕ (top), and the velocity $\mathbf{v}$ (bottom) at time $t = 11.25$ for $\theta = 0°$, $\theta = 20°$, $\theta = 45°$, and $\theta = 60°$ (from left to right), with the respective values $\|\mathbf{v}(11.25)\| = 4.53 \times 10^{-4}$, 6.37×10^{-2}, 2.70×10^{-2}, and 2.07×10^{-2}.

8. Concluding remarks

We have presented a conservative MR finite-volume scheme for the numerical approximation of velocity, pressure and solids volume fraction of the sedimentation of a suspension in inclined channels. This simple rectangular geometry has been chosen for the obvious ease of implementation of the finite volume scheme and the multiresolution method. Clearly, this FV-MR method is also of interest for more involved geometries. Few modifications are necessary to adapt it to two-dimensional vessels that are defined by combinations of rectangles (cf., e.g., [49]).

The underlying model simply consists in a conservation law for the concentration coupled with a modified version of the Stokes system for the flow. The MR approach was applied to accurately resolve the sharp fronts arising in the concentration field

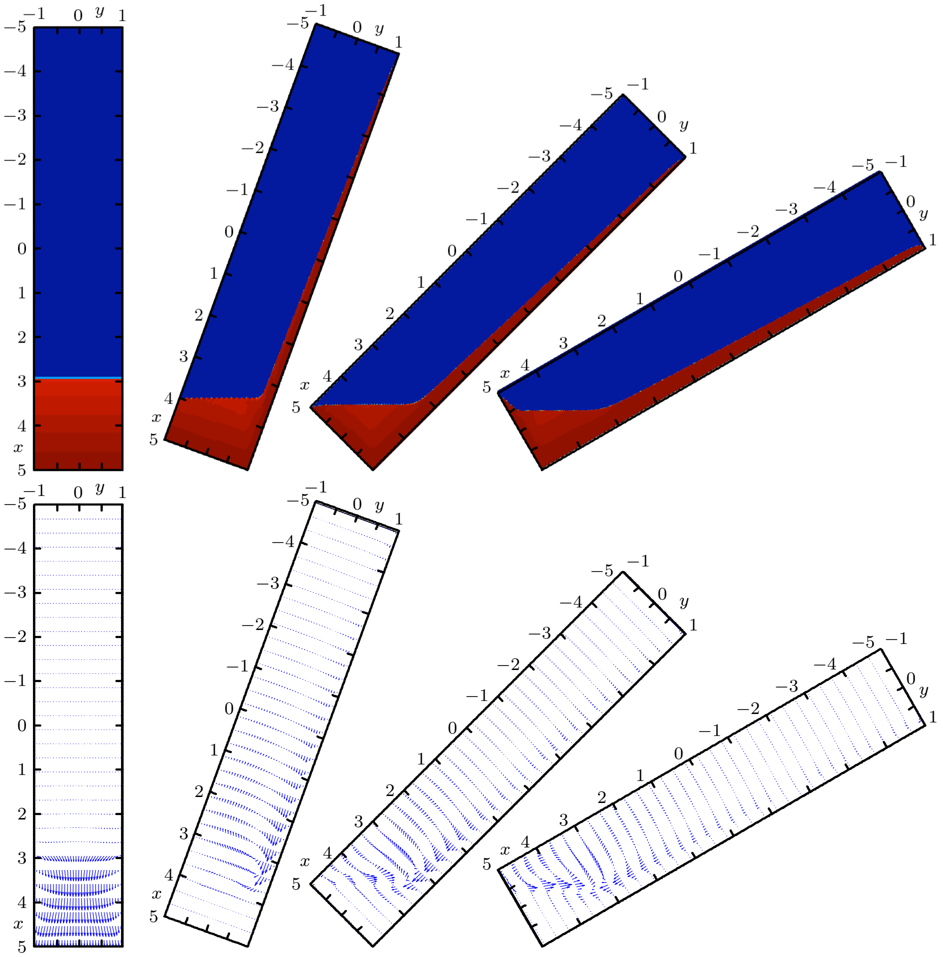

FIGURE 19. Example 6 (coupled problem, $L = 8$, $\eta^2 = 1/9000$): numerical solution for the concentration ϕ (top), and the velocity $\mathbf{v}$ (bottom) at time $t = 16$ for $\theta = 0°$, $\theta = 20°$, $\theta = 45°$, and $\theta = 60°$ (from left to right), with the respective values $\|\mathbf{v}(16)\| = 9.85 \times 10^{-5}$, 2.36×10^{-2}, 1.43×10^{-2}, and 1.35×10^{-2}.

while allowing for data and CPU time compression. To avoid spurious oscillations in the pressure, the Stokes system is solved using a pressure-stabilized method.

Several improvements are envisaged from both modeling and numerical aspects. First, we would like to include a degenerate diffusive term in the concentration equation, in order to be able to model flocculated suspensions including the effect of sediment compressibility [4, 13]. In the same line, the extension to polydisperse suspensions would be of interest to us (see [11] and references cited in that paper). On the other hand, we want to explore the behavior of the enhanced sedimentation in different flow regimes. There, more suitable models for the flow field will be needed, such as the full Navier-Stokes equations coupled if necessary with a k-ϵ turbulence model. Regarding numerics, an important pending task consists in constructing an adequate MR analysis for the Stokes or Navier-Stokes equations, and developing robust coupling methodologies. More straightforward extensions include the incorporation of high-order and/or adaptive schemes for the time discretization (as done for instance in 1D models of sedimentation [15]), or performing semi-implicit methodologies to decouple the advection steps constrained by the CFL condition from those given by the Stokes solver, and therefore using larger time steps for the flow equations (see e.g. [43]).

Acknowledgments

RB acknowledges support by Conicyt (Chile) through Fondecyt project 1090456, BASAL project CMM, Universidad de Chile and Centro de Investigación en Ingeniería Matemática (CI^{2}MA), Universidad de Concepción. RR acknowledges financial support by the European Research Council through the advanced grant "Mathcard, Mathematical Modelling and Simulation of the Cardiovascular System", ERC-2008-AdG 227058 and by the postdoctoral grant "Becas Chile". HT is supported by Mecesup project UCO0713 and acknowledges the hospitality of M2P2-CNRS, Université de Provence, Marseille (France). KS thankfully acknowledges financial support from the PEPS program of INSMI-CNRS.

References

[1] Acrivos, A. and Herbolzheimer, E., Enhanced sedimentation in settling tanks with inclined walls, J. Fluid Mech., 92 (1979) 435–457.
[2] Amberg, G. and Dahlkild, A.A., Sediment transport during unsteady settling in an inclined channel, J. Fluid Mech., 185 (1987) 415–436.
[3] Bendahmane, M., Bürger, R., and Ruiz-Baier, R., Multiresolution space-time adaptive scheme for the bidomain model in electrocardiology, Numer. Meth. Partial Diff. Eqns., 26 (2010) 1377–1404.
[4] Berres, S., Bürger, R., Karlsen, K.H., and Tory, E.M., Strongly degenerate parabolic-hyperbolic systems modeling polydisperse sedimentation with compression, SIAM J. Appl. Math., 64 (2003) 41–80.
[5] Bihari, B.L. and Harten, A., Multiresolution schemes for the numerical solution of 2-D conservation laws I, SIAM J. Sci. Comput., 18 (1997) 315–354.
[6] Blanchette, F., Peacock, T., and Bush, J.W.M., The Boycott effect in magma chambers, Geophys. Res. Letters, 31 (2004) L05611.
[7] Borhan, A. and Acrivos, A., The sedimentation of nondilute suspensions in inclined settlers, Phys. Fluids, 31 (1988) 3488–3501.
[8] Boycott, A.E., Sedimentation of blood corpuscles, Nature 104 (1920) 532.
[9] Brezzi, F. and Pitkäranta, J., On the stabilization of finite element approximations of the Stokes equations, in Efficient Solutions of Elliptic Systems, Kiel, 1984, Notes Numer. Fluid Mech. 10, Vieweg, Braunschweig, Germany, 1984, 11–19.
[10] Brinkman, H.C., The viscosity of concentrated suspensions and solutions, J. Chem. Phys., 20 (1952) 571.
[11] Bürger, R., Donat, R., Mulet, P., and Vega, C.A., Hyperbolicity analysis of polydisperse sedimentation models via a secular equation for the flux Jacobian, SIAM J. Appl. Math., 70 (2010) 2186–2213.
[12] Bürger, R., and Kozakevicius, A., Adaptive multiresolution WENO schemes for multi-species kinematic flow models, J. Comput. Phys., 224 (2007) 1190–1222.
[13] Bürger, R. and Kunik, M., A critical look at the kinematic-wave theory for sedimentation-consolidation processes in closed vessels, Math. Meth. Appl. Sci., 24 (2001) 1257–1273.
[14] Bürger, R., Ruiz-Baier, R., and Schneider, K., Adaptive multiresolution methods for the simulation of waves in excitable media, J. Sci. Comput., 43 (2010) 261–290.
[15] Bürger, R., Ruiz-Baier, R., Schneider, K., and Sepúlveda, M., Fully adaptive multiresolution schemes for strongly degenerate parabolic equations in one space dimension, M2AN Math. Model. Numer. Anal., 42 (2008) 535–563.
[16] Bürger, R. and Tory, E.M., On upper rarefaction waves in batch settling, Powder Technol., 108 (2000) 74–87.
[17] Bürger, R., Wendland, W.L., and Concha, F., Model equations for gravitational sedimentation-consolidation processes, ZAMM Z. Angew. Math. Mech., 80 (2000) 79–92.

[18] Bustos, M.C., Concha, F., Bürger, R., and Tory, E.M. Sedimentation and Thickening, Kluwer Academic Publishers, Dordrecht, 1999.

[19] Chiavassa, G., and Donat, R., Point value multiresolution for 2D compressible flows, SIAM J. Sci. Comput., 23 (2001) 805–823.

[20] Chun-Liang, W. and Jie-Min, Z., Eulerian simulation of sedimentation flows in vertical and inclined vessels, Chin. Phys., 14 (2005) 620–628.

[21] Cohen, A., Kaber, S., Müller S., and Postel, M., Fully adaptive multiresolution finite volume schemes for conservation laws, Math. Comp., 72 (2003) 183–225.

[22] Dahmen, W., Gottschlich-Müller, B., and Müller, S., Multiresolution schemes for conservation laws, Numer. Math., 88 (2001) 399–443.

[23] Davis, R.H. and Acrivos, A., Sedimentation of noncolloidal particles at low Reynolds numbers, Ann. Rev. Fluid Mech., 17 (1985) 91–118.

[24] Doroodchi, E., Fletcher, D.F., and Galvin, K.P., Influence of inclined plates on the expansion behaviour of particulate suspensions in a liquid fluidised bed, Chem. Eng. Sci., 59 (2004) 3559–3567.

[25] Eymard, R., Gallouët, T., and Herbin, R., Finite Volume Methods. In: P.G. Ciarlet, J.L. Lions (eds.), Handbook of Numerical Analysis, vol. VII, North-Holland, Amsterdam, 2000, pp. 713–1020.

[26] Eymard, R., Herbin, R., and Latché, J.C., Convergence analysis of a colocated finite volume scheme for the incompressible Navier-Stokes equations on general 2 or 3D meshes, SIAM J. Numer. Anal., 45 (2007) 1–36.

[27] Fischer, P., Bruneau, C.H., and Kellay, H., Multiresolution analysis for 2D turbulence. Part 2: a physical interpretation, Discr. Cont. Dyn. Syst., 7 (2007) 717–734.

[28] Galvin, K.P. and Nguyentranlam, G., Influence of parallel inclined plates in a liquid fluidized bed system, Chem. Eng. Sci., 57 (2002) 1231–1234.

[29] Galvin, K.P., Callen, A., Zhou, J., and Doroodchi, E., Performance of the reflux classifier for gravity separation at full scale, Minerals Eng., 18 (2005) 19–24.

[30] Graham, W. and Lama, R., Sedimentation in inclined vessels, Canad. J. Chem. Engrg., 41 (1963) 31–32.

[31] Graham, W. and Lama, R., Continuous thickening in an inclined thickener, Canad. J. Chem. Engrg., 41 (1963) 162–165.

[32] Harten, A., Multiresolution algorithms for the numerical solution of hyperbolic conservation laws, Comm. Pure Appl. Math., 48 (1995) 1305–1342.

[33] Herbolzheimer, E. and Acrivos, A., Enhanced sedimentation in narrow tilted channels, J. Fluid Mech., 108 (1981) 485–499.

[34] Kerr, O.S., An exact solution in sedimentation under an inclined wall, Phys. Fluids, 18 (2006), paper 128101.

[35] Kynch, G.J., A theory of sedimentation., Trans. Faraday Soc., 48 (1952) 166–176.

[36] Latsa, M., Assimacopoulos, D., Stamou, A., and Markatos, N., Two-phase modeling of batch sedimentation, Appl. Math. Model., 23 (1999) 881–897.

[37] Laux, H., Ytrehus, T., Computer simulation and experiments on two-phase flow in an inclined sedimentation vessel, Powder Technol., 94 (1997) 35–49.

[38] Madge, D.N., Romero, J., and Strand W.L., Process reagents for the enhanced removal of solids and water from oil sand froth, Minerals Eng., 18 (2005) 159–169.

[39] McCaffery, S.J., Elliott, L., and Ingham, D.B., Two-dimensional enhanced sedimentation in inclined fracture channels, Math. Engrg., 7 (1998) 97–125.

[40] Müller, S., Adaptive Multiscale Schemes for Conservation Laws. Springer-Verlag, Berlin, 2003.

[41] Müller, S. and Stiriba, Y., Fully adaptive multiscale schemes for conservation laws employing locally varying time stepping, J. Sci. Comput., 30 (2007) 493–531.

[42] Nakamura, H. and Kuroda, K., La cause de l'accélération de la vitesse de sédimentation des suspensions dans les récipients inclinés, Keijo J. Medicine, 8 (1937) 256–296.

[43] Nigam, M.S., Numerical simulation of buoyant mixture flows, Int. J. Multiphase Flow, 29 (2003) 983–1015.

[44] Oliver, D.R., Continuous vertical and inclined settling of model suspensions, Canad. J. Chemical Engrg., 42 (1964) 268–272.

[45] Oliver, D.R. and Jenson, V.G., The inclined settling of dispersed suspensions of spherical particles in square-section tubes, Canad. J. Chemical Engrg., 42 (1964) 191–195.

[46] Pabst, W., Fundamental considerations on suspension rheology, Ceramics-Silikáty, 48 (2004) 6–13.

[47] Pearce, K.W., Settling in the presence of downward-facing surfaces. in: Proceedings of the Symposium on the Interaction between Fluids and Particles, London, 20–22 June 1962. Instn. Chem. Engrs. (London), 1962, pp. 30–39.

[48] Ponder, P., On sedimentation and rouleaux formation, Quart. J. Exper. Physiol., 15 (1925) 235–252.

[49] Rao, R.R., Mondy, L.A., and Altobelli, S.A., Instabilities during batch sedimentation in geometries containing obstacles: a numerical and experimental study, Int. J. Numer. Meth. Fluids, 55 (2007) 723–735.

[50] Richardson, J.F. and Zaki, W.N., Sedimentation and fluidization: Part I, Trans. Instn. Chem. Engrs. (London), 32 (1954) 35–53.

[51] Roscoe, R., The viscosity of suspensions of rigid spheres, Brit. J. Appl. Phys., 3 (1952) 267–269.

[52] Roussel, O., Schneider, K., Tsigulin A., and Bockhorn, H., A conservative fully adaptative multiresolution algorithm for parabolic PDEs, J. Comput. Phys., 188 (2003) 493–523.

[53] Santos, J.C., Crus, P., Alves, M.A., Oliveira, P.J., Magalhães, F.D., and Mendes, A., Adaptive multiresolution approach for two-dimensional PDEs, Comput. Methods Appl. Mech. Engrg., 193 (2004) 405–425.

[54] Schaflinger, U., Experiments on sedimentation beneath downward-facing inclined walls, Int. J. Multiphase Flow, 11 (1985) 189–199.

[55] Schneider, W., Kinematic-wave theory of sedimentation beneath inclined walls, J. Fluid Mech., 120 (1982) 323–346.

[56] Shaqfeh, E.S.G. and Acrivos, A., The effects of inertia on the buoyancy-driven convective flow in settling vessels having inclined walls, Phys. Fluids, 29 (1986) 3935–2948.

[57] Shaqfeh, E.S.G. and Acrivos, A., The effects of inertia on the stability of the convective flow in inclined plate settlers, Phys. Fluids, 30 (1987) 960–973.

[58] Shaqfeh, E.S.G. and Acrivos, A., Enhanced sedimentation in vessels with inclined walls: experimental observations, Phys. Fluids, 30 (1987) 1905–1914.

[59] Sjögreen, B., Numerical experiments with the multiresolution scheme for the compressible Euler equations, J. Comput. Phys., 117 (1995) 251–261.

[60] Tory, E.M. (ed.), Sedimentation of Small Particles in a Viscous Fluid, Computational Mechanics Publications, Southampton, 1996.

[61] Ungarish, M., Hydrodynamics of Suspensions. Springer-Verlag, Berlin, 1993.

[62] Wan, T., Aliabadi, S., and Bigler, C., A hybrid scheme based on finite element/volume methods for two immiscible flows, Int. J. Numer. Meth. Fluids, 61 (2009) 930–944.

[63] Zahavi, E. and Rubin, E., Settling of suspensions under and between inclined surfaces, Ind. Eng. Chem. Process Des. Develop., 14 (1975) 34–41.

CI^{2}MA and Departamento de Ingeniería Matemática, Facultad de Ciencias Físicas y Matemáticas, Universidad de Concepción, Casilla 160-C, Concepción, Chile
E-mail: `rburger@ing-mat.udec.cl`

Modeling and Scientific Computing, MATHICSE, Ecole Polytechnique Fédérale de Lausanne EPFL, Station 8, CH-1015, Lausanne, Switzerland
E-mail: `ricardo.ruiz@epfl.ch`

M2P2-CNRS and Centre de Mathématiques et d'Informatique, Université de Provence, 39 rue Joliot-Curie, 13453 Marseille cedex 13, France
E-mail: `kschneid@cmi.univ-mrs.fr`

Departamento de Matemáticas, Facultad de Ciencias, Universidad de La Serena, Av. Cisternas 1200, La Serena, Chile
E-mail: `htorres@ing-mat.udec.cl`